Chapter 9
Implementation of Rod Vortex Generators on Helicopter Rotor Blades in Hover and Forward Flight Conditions

Fernando Tejero, Piotr Doerffer, Paweł Flaszyński, and Oskar Szulc

Nomenclature

Latin

c	Airfoil chord [m]
C_p	Pressure coefficient [-]
C_q	Torque coefficient [-]
C_T	Thrust coefficient [-]
h	Height of the rod [m]
L	Distance between VGs [m]
M	Mach number [-]
M_T	Tip Mach number [-]
R	Rotor radius [m]
Re_T	Tip Reynolds number [-]
V_∞	Forward speed [km/h]
y^+	Non dimensional distance to the wall [-]

Greek

δ	Boundary layer thickness [m]
ϕ_{RVG}	Diameter of the RVG [m]

F. Tejero (✉) • P. Doerffer • P. Flaszyński • O. Szulc
Institute of Fluid Flow Machinery Polish Academy of Sciences, Gdansk, Poland
e-mail: fernando.tejero@imp.gda.pl

P. Doerffer et al. (eds.), *Recent Progress in Flow Control for Practical Flows*,
DOI 10.1007/978-3-319-50568-8_9

ψ	Rotor azimuth [°]
θ	Blade collective [°]

Acronyms

AR	Aspect ratio
CFD	Computational fluid dynamics
CFL	Courant–Friedrichs–Lewy
C–T	Caradonna–Tung
RANS	Reynolds-averaged Navier–Stokes
RPM	Revolutions per minute
RVG	Rod vortex generator

9.1 Introduction

Based on the success of simple configurations, the application of flow control systems in more realistic geometries has also been recently considered. Several techniques have been investigated in rotorcraft applications (particularly in helicopters). The main feature of the aerodynamics of a helicopter is the unsteadiness of the flow due to its rotating parts (i.e., main and tail rotors). The non-rotating part of the helicopter, mainly the fuselage, is also exposed to large areas of reverse flow. In high-speed forward flight conditions, the massive flow separation present at the rear of the fuselage is the major component of the parasitic drag of the helicopter. In this respect, separation control for drag reduction purposes has been investigated over the past years by means of vortex generators, synthetic jets, or steady blowing (Boniface 2014)

On the rotating parts of the helicopter (main rotor blade), different flow control system might be suitable to implement. A typical aerodynamic environment for the helicopter main rotor in forward flight is shown in Fig. 9.1. On the advancing side ($0° < \psi < 180°$), the forward velocity is added to the blade's rotational velocity while on the retreating side ($180° < \psi < 360°$), the forward velocity is subtracted from the blade rotation. This unsteadiness of the flow leads to compressibility effects on the advancing side due to high Mach numbers while blade stall might be present on the retreating side if the forward flight velocity is high enough. For example, shock-wave induced flow separation on the advancing side may be controlled by vortex generators while the massive separation caused by dynamic stall may be controlled by Gurney flaps. It is important to mention that passive flow control systems (e.g., vortex generators) could be implemented in the rotor blades where they would work properly in some azimuthal positions with some drawbacks in others. For this reason, a passive system could be activated on demands. On the other hand, active flow control systems are suitable for helicopter application since they are just enabled for certain azimuthal range.

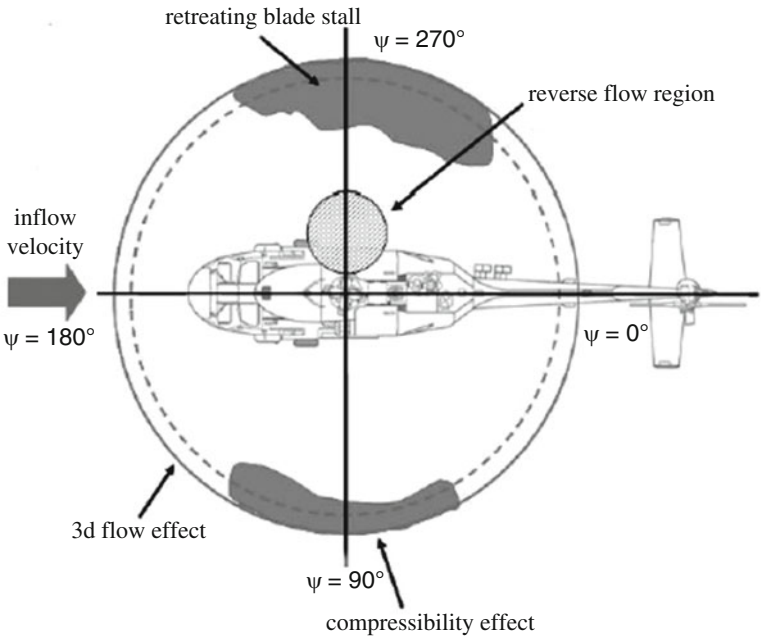

Fig. 9.1 Flow characteristics in forward flight conditions (Seddon and Newman 2011)

A list of different flow control devices have been identified as candidates to be integrated in helicopter rotor blades: vortex generators, gurney flaps, movable flaps, surface blowing circulation control, synthetic jets, surface suction, passive porous or slotted surfaces, bumps or localized shaping, and riblets. The principles of each device, with the main benefits for rotorcraft application, were recently published by Kenning et al. (2004).

9.2 Numerical Model

The numerical model as well as computational domain employed in these simulations was previously described in Tejero et al. (2016a). The present CFD investigation was carried out using the DLR (Germany) FLOWer solver. It is a rotorcraft oriented, block-structured, cell-centered code which solves the Reynolds-averaged Navier–Stokes (RANS) equations with several closures. The two-equation, LEA k–ω turbulence model was used due to its capabilities for proper prediction of transonic flows. The numerical algorithm is based on a semidiscrete approach, utilizing a finite-volume, central scheme (second order) for the spatial discretization. The same explicit, Runge–Kutta method of time integration, was used for the steady simulations of a hovering rotor, as for the internal iterations of the implicit

dual-time-stepping scheme (second order) applied for forward flight conditions. Same numerical algorithm was used in previous investigations.

The main idea of the chimera technique implemented in the ROT/CHIMERA version of the FLOWer code is to easily generate grids for complex configurations (e.g., helicopter rotors) by decomposing them into simple, independent parts. For the reference case (no flow control), the computational domain consists of a background and the blade component grids. The RVGs component grid is added for each blade to the reference setup for the flow control case.

In hovering rotor computations, the background component grid is formed by a cylinder of a height and radius equal to 6.1R and 4.0R, respectively, which ensures that the rotor blades are located at least 3.0R from the outer boundary of the domain. Altogether, 32 computational blocks contain 4.80×10^6 volumes. The vicinity of the rotor and its wake is resolved using a central cuboid structure with a uniform block (volume size of $0.1c \times 0.1c \times 0.1c$). For forward flight simulations, a Cartesian, cuboid background component grid (see Fig. 9.2) is designed with dimensions of $16.4R \times 18.2R \times 18.2R$. Consequently, the outer boundary of the domain is positioned at least 8.0R from the rotor in all directions. The number of control volumes in 32 computational blocks is increased to 9.4×10^6, much higher than for the hover setup. Again, the vicinity of the rotor is resolved using a central cuboid structure with uniform volume distribution ($0.1c \times 0.1c \times 0.1c$). For both states of flight, the blade component grid (Fig. 9.3) is C-type in streamwise

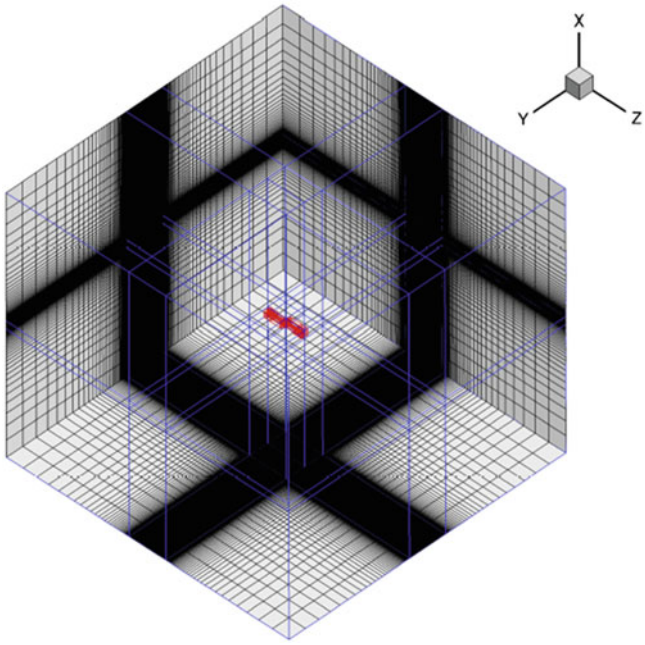

Fig. 9.2 Background component grid

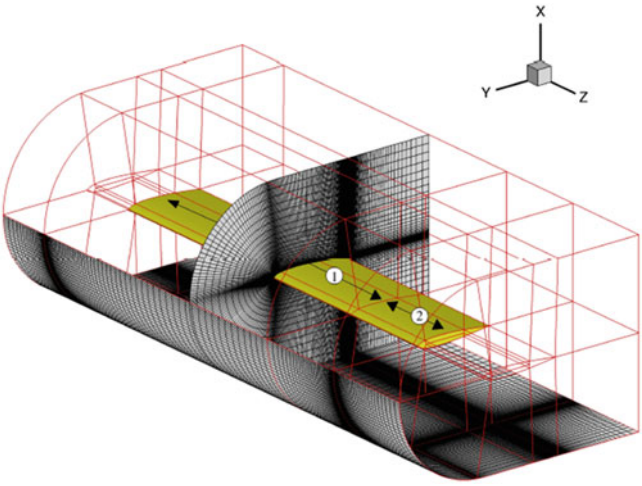

Fig. 9.3 Blade component grid

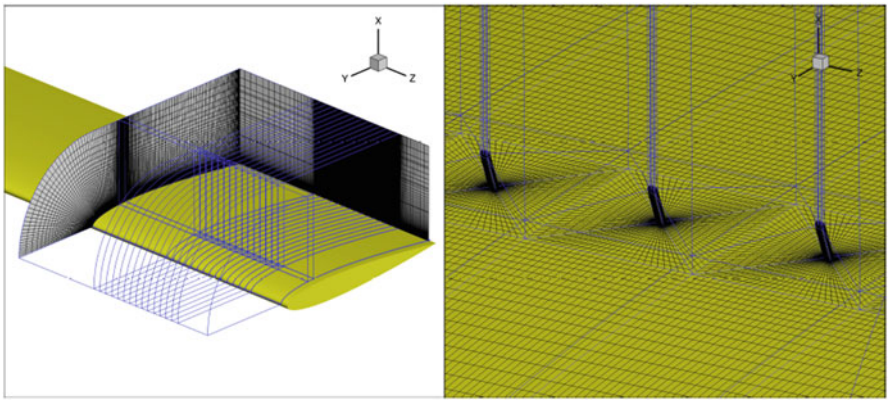

Fig. 9.4 RVG component grid and detailed view of the RVGs

and H-type in crosswise directions. It extends 1.2c from the blade surface in the radial and normal directions. Altogether, 40 computational blocks contain 3.9×10^6 volumes per blade.

The nondimensional distance of the first layer of cells from the solid surface of the blade is of the order $y^+ = 1$. For the flow control cases, an RVG component grid (Fig. 9.4) is added to the chimera setup. It is placed on the suction side of the blade, near the tip, where there is a significant flow separation.

Three types of boundary conditions are applied in the numerical simulation: no-slip condition with zero heat flux (adiabatic) at the rotor blades, Froude (hover), and far-field (forward flight) at the external edges of the background grids, and a

special chimera condition at the outer part of the blade component grids, which is necessary for the accurate interpolation process of flow variables between meshes.

The inclusion of the RVGs component grid leads to a significant increase of the mesh size, making the simulations computationally very demanding (37×10^6 volumes for hover and 48×10^6 volumes for forward flight conditions).

9.3 Hover Conditions

9.3.1 Experimental Data

The experimental data obtained by Caradonna and Tung (C–T), Caradonna and Tung (1981), is the first test data available in the literature that combines measurements of static pressure on the blade and tip vortex trajectory (see Fig. 9.5). The data was gathered in the Army Aeromechanics Laboratory's hover test facility in the 1980s. The model rotor employed two cantilever mounted, rectangular, untwisted, and untapered NACA0012 rigid blades. The rotor was mounted on a tall column containing a drive shaft with half degree precone angle and located in the center of a large chamber with special ducting designed to eliminate room recirculation. The diameter of the rotor was 7.5 ft (2.286 m) and the chord length was 0.625 ft (0.1905 m) leading to a rotor aspect ratio of 6.0. Different rotational speeds of the rotor were applied during the experiments (from 650 RPM to 2540 RPM) which varied the tip Mach number from 0.226 to 0.890. The collective pitch ranged between 0° and 12°. Each blade was mounted with 60 pressure tubes which permits to measure five different locations—three radial locations per blade with one common. The static pressure was recorded at $r/R = 0.50$, 0.68, 0.80, 0.89, and 0.96. On the other hand, the wake data was acquired with a hot-wire probe mounted beneath the rotor.

9.3.2 CFD Results

9.3.2.1 Reference Case

The FLOWer code has been validated with a high-speed transonic case of $M_T = 0.877$, $Re_T = 3.93 \times 10^6$ and a collective pitch of $\theta = 8°$. Same flow conditions have been analyzed by other researchers in the past using Euler and/or RANS approach and with/without wake models. A literature survey of the RANS results obtained for this transonic lifting hover reveals significant scatter according to experimental data (Kang and Kwon 2002; Sheng 2011).

As mentioned above, the correct prediction of the flow-field around the rotor blades requires properly resolved flow structure details. The properly captured rotor wake and the tip vortex path are necessary condition for the correct prediction of the

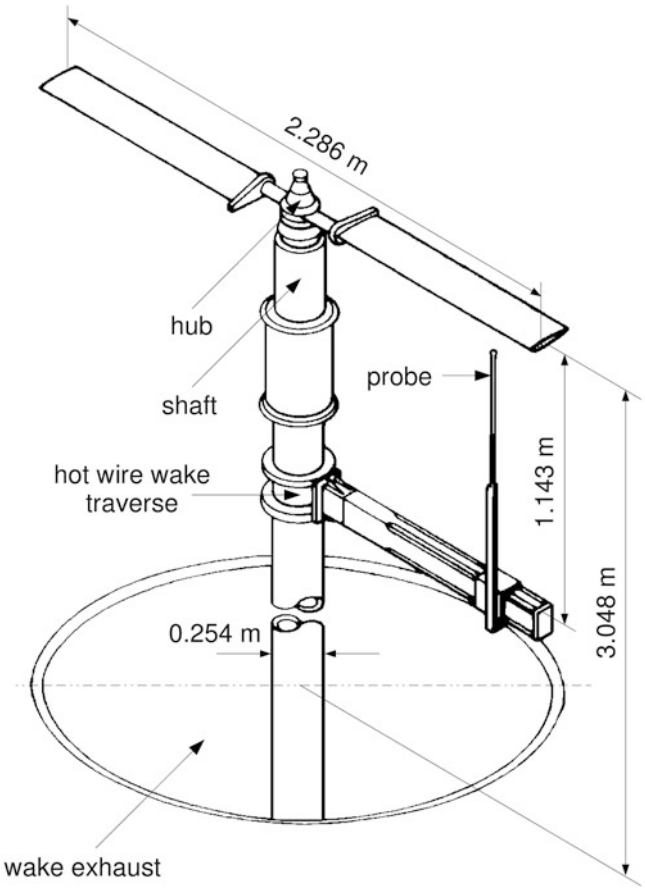

Fig. 9.5 Caradonna and Tung model helicopter rotor blade (Caradonna and Tung 1981)

rotor performance. In the present study, the rotor wake is not set externally by a wake model but it is a result of the simulation. A strong, induced vertical inflow modifies the effective angle of attack of the blades directly altering the rotor performance.

Approximately 450° of a tip vortex age is resolved in the current simulation, which is sufficient to capture the interaction of the shed vortex with the following blade at 180°. The tip vortices and trailing edge vortex sheets are diffused mainly due to the numerical viscosity of the second order central scheme applied. Below 180° the tip vortex descent and contraction rate (based on the location of the vorticity maximum) is accurately predicted by the solver FLOWer (Fig. 9.6). It is important to mention that after half rotation, the accuracy of the simulation with respect to experimental data decreases due to the wake traveling far from the wake box prepared in the background component grid.

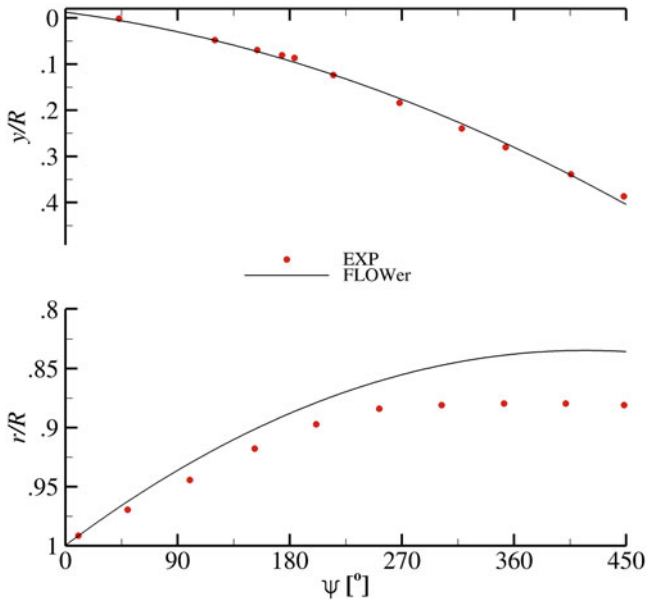

Fig. 9.6 Tip vortex descent and contraction for the C–T model rotor in transonic conditions

Figure 9.7 presents the validation of the numerical simulation in terms of comparison of pressure coefficient distributions at different cross-section in radial ($r/R = 0.50$, 0.68, 0.80, 0.89, and 0.96). The flow is fully subsonic at the first two cross-sections ($r/R = 0.50$ and 0.68) and supersonic areas terminated by shock waves appear at the remaining sections ($r/R = 0.80$, 0.89, and 0.96). Although there is a satisfactory agreement with the experimental C_p distributions, there is an overprediction of thrust coefficient by 15% ($C_T = 0.00545$) compared to the published value ($C_T = 0.00473$).

$$c_T = \frac{T}{\frac{1}{2}\rho A V_{\text{tip}}^2} \tag{9.1}$$

The strong shock wave at the tip of the rotor blade induces flow separation between $r/R = 0.86$ and 0.96 (with detachment line located at $x/c = 0.30$). Due to previous chapter proven that RVGs are able to control flow separation, the implementation of this flow control device on helicopter rotor blades in hover conditions will be investigated in this chapter. Upstream of the separation bubble ($x/c = 0.20$), the boundary layer thickness was 0.008c. As suggested in the previous chapter, the dimensions of the rod vortex generators were: $\phi_{\text{RVG}} = \delta/4$, $h = \delta/2$, and $L = 2.5 \times \delta$. The spacing between the rods was increased to $L = 5 \times \delta$, reducing the total number of control volumes (14 rods are simulated instead of 28).

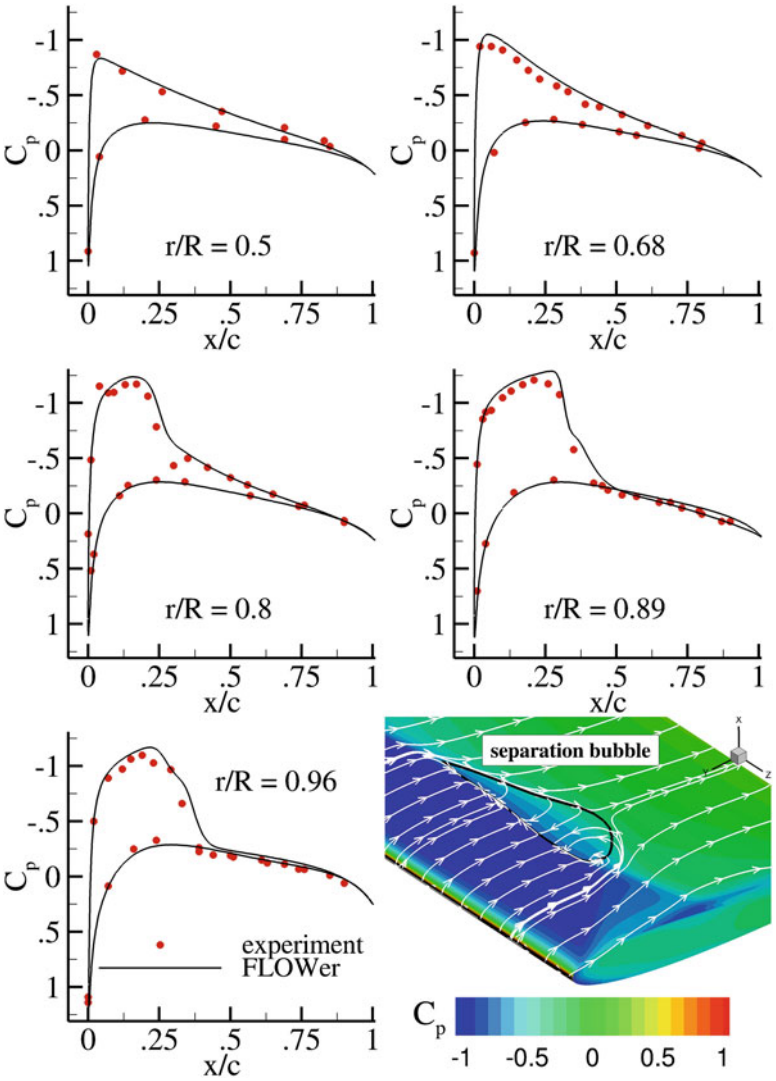

Fig. 9.7 Numerical validation of the C–T model rotor in transonic conditions and separation bubble (Tejero et al. 2016a)

9.3.2.2 Flow Control Case (RVG)

Figure 9.8 presents the development of the streamwise vortices created by the RVGs on the C–T helicopter rotor blade at five chordwise sections ($x/c = 0.22$, 0.25, 0.27, 0.29, and 0.33). It is worth to mention that the effect of the RVGs is only visible below the edge of the boundary layer thickness where the vortex generators are submerged. For the chordwise sections upstream of the separation bubble

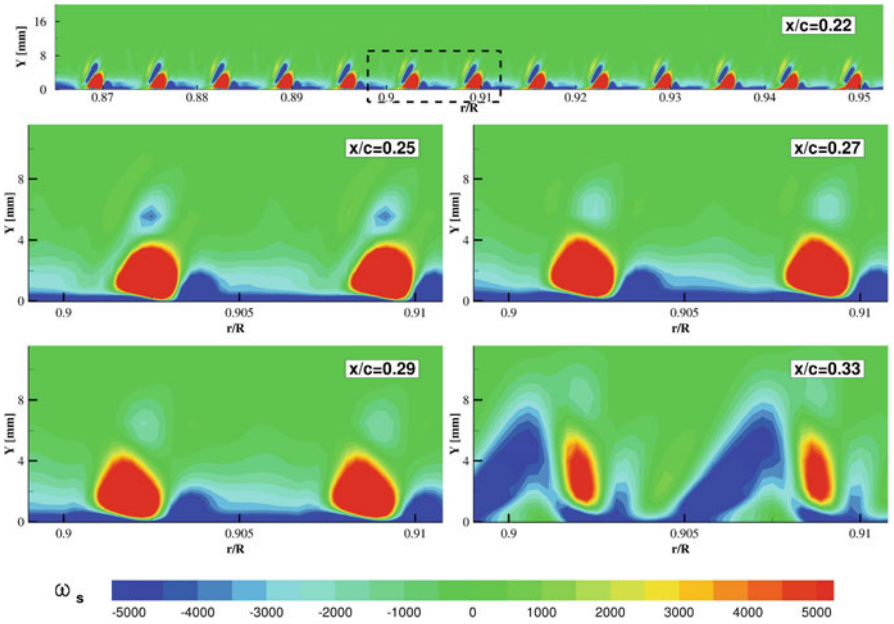

Fig. 9.8 Streamwise vortex development in the C–T model rotor in transonic conditions

($x/c = 0.22$, 0.25, 0.27, and 0.29), the vortex develops increasing the intensity. On the other hand, when the flow separations starts ($x/c = 0.30$), the vortex core is lifted and highly dissipated (see Fig. 9.8 chordwise section $x/c = 0.33$). The numerical simulation reveals that there is a very weak vortex downstream of the reattachment point.

The numerical results of the flow past the rotor blade with the proposed passive flow control system show the possibility of reduction of the separation bubble (Fig. 9.9). The figure presents the contour map of skin friction coefficient C_f, the separation bubble (black line) and the low momentum area (red line) are marked in the figure. The proposed vortex generators increase the shear stress at the suction side of the rotor blade due to the formation of streamwise vortices. The separation bubble is not fully eliminated but reduced and spit into smaller bubbles which follow the same trends presented in channel flows and airfoils (previous chapter).

In Fig. 9.10 the boundary layer profiles are compared for the reference and flow control cases (all analyzed points are marked in Fig. 9.9). The solid lines represent a location downstream of a selected RVG ($r/R = 0.911$), while the dashed lines refer to a downstream position between two rods ($r/R = 0.922$) at four different chordwise sections ($x/c = 0.25$, 0.35, 0.40, and 0.60). The first chordwise section ($x/c = 0.25$) is located upstream of the starting point of the flow separation, the other two sections ($x/c = 0.35$ and 0.40) refer to locations where reverse flow is present while the flow is attached to the blade for the last analyzed chordwise section ($x/c = 0.60$). The comparison of boundary layer profiles at $x/c = 0.25$ shows a big influence in the

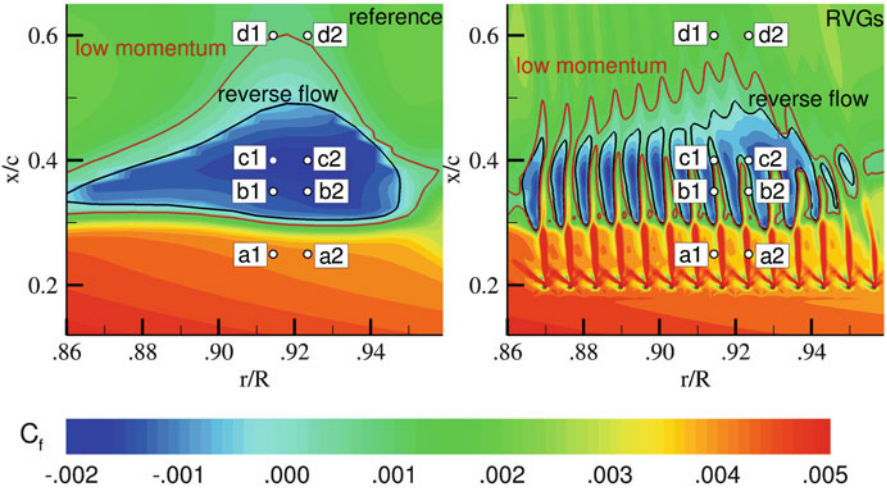

Fig. 9.9 Flow separation reduction by RVGs on the C–T model rotor in transonic conditions

radial section downstream of the rod (solid line) providing a more full profile when the proposed flow control system is applied while the boundary layer properties are similar for the radial section located between RVGs (dashed line). Traveling downstream in chordwise direction ($x/c = 0.35$), the flow separation appears in the reference case but in case of applied RVG the flow is attached in both radial sections. The other positive effect of vortex generator can be observed at $x/c = 0.40$. Although the flow is not attached at $r/R = 0.92$, the height of the separation bubble is reduced. The comparison makes evident that not only the area of the projection of the separation bubble on the surface is reduced but also the height of it. Lastly, when the flow is reattached for the reference case ($x/c = 0.60$), the effect of the streamwise vortex has been dissipated making similar boundary layer profiles for the reference and flow control cases.

The implementation of the passive flow control device of rod vortex generators on the tip of the C–T model rotor blade in transonic hover conditions increases the thrust coefficient C_T by 2.0 % with respect to the reference case. The main drawback of this technology is the drag penalty associated with it (the power consumption was increased by 1.2 %). The separation bubble induced at the tip of these rotor blades by a strong shock wave was limited by the proposed technology.

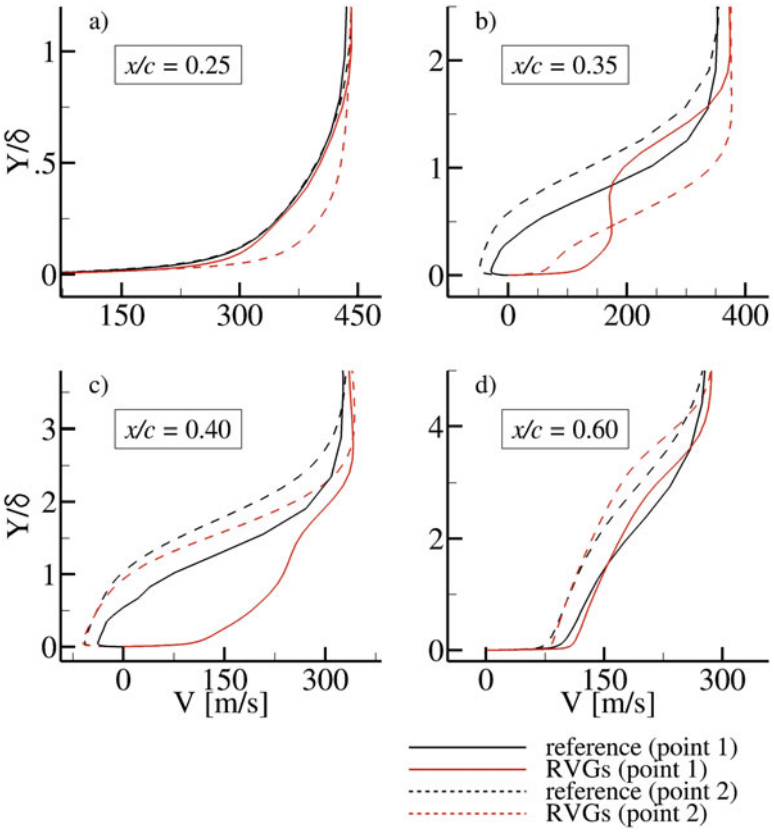

Fig. 9.10 Comparison of boundary layer thickness

9.4 Forward Flight Conditions

9.4.1 Flight Test Data

The AH-1G helicopter rotor blade (Fig. 9.11) was selected for the numerical investigation of the forward flight conditions. During The Tip Aerodynamics and Acoustics Test (TAAT), performed by Cross and Watts (1988), several arrays of absolute pressure transducers were placed on the rotor blades providing a large set of data. This flight test campaign is one of the most detailed one that can be found in the open literature so far. The data includes overall instantaneous thrust coefficients C_T, torque coefficient C_q, and the sectional normal force coefficients C_n based on the integration of the pressure data collected from the pressure transducers located on the blade. Besides, the blade motion (pitch and flap) was recorded as well.

The AH-1G is a two person, single-engine helicopter that first flew in 1965 and has been out of service for 20 years. The AH-1G 2-bladed, teetering rotor with a 540

Fig. 9.11 AH-1G helicopter rotor blade (www.airliners.net)

symmetrical airfoil section, which is a highly modified derivative of the NACA 0012 (thickness ratio = 0.0933), has a rectangular planform with a chord $c = 0.686$ m. The blades have a linear twist of $-10°$ from the shaft to the tip (effective twist from blade root to tip is $-8.48°$) with a radius $R = 6.71$ m (aspect ratio AR = 9.8). During the TAAT test, the effective chord of the blade was increased to accommodate the instrumentation sleeve, reducing the effective aspect ratio to 9.2.

A literature survey of the published numerical results (Ahmad and Duque 1996; Yang et al. 2002) for the TAAT AH-1G campaign reveals that the low-speed flight ($V_\infty = 150$ km/h) has been simulated in the past by several researchers with success, in contrast to the higher speed flight test points where CFD calculations are very limited (i.e., medium- and high-speed flights with forward velocities of $V_\infty = 210$ km/h and 290 km/h, respectively). After the TAAT flight test campaign, one hover IGE (test point no. 2370) and six forward flight cases (test points no. 2152–2157) with increasing forward speeds (from 150 km/h to 290 km/h) were documented in Cross and Watts (1988). This section presents exemplary numerical results obtained for a subset of 3 test points. Test point no. 2157 (low-speed case, 150 km/h) was computed and validated against flight test data and compared with other CFD results found in the literature (i.e., Ahmad and Duque 1996; Yang et al. 2002). Two higher speed test cases investigated do not have similar citations available in the literature. Numerical results for test point no. 2152 (high-speed, 290 km/h) are satisfactory in terms of flight test data comparison revealing significant flow separation (shock wave induced at the advancing side and due to dynamic stall at the retreating side) (Tejero et al. 2016a, b).

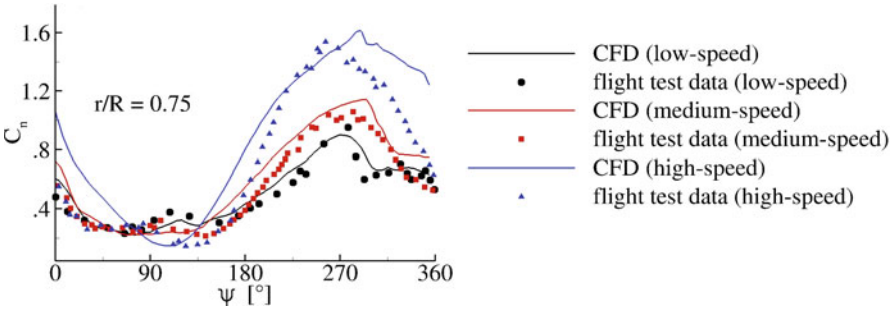

Fig. 9.12 Instantaneous normal C_n coefficient for different speed markers

9.4.2 CFD Results

9.4.2.1 Reference Case

The thrust coefficient is only overpredicted by 2 % for the low-speed case ($C_T = 0.00473$), while the overprediction increases with the forward speed: 9 % ($C_T = 0.00507$) for the medium-speed and 20 % ($C_T = 0.00569$) for the high-speed marker. Nevertheless, the agreement is satisfactory for the complex flow conditions simulated and simplifications undertaken (e.g., neglect the influence of the fuselage). It is important to mention that during the simulations, the blade motion reported in TAAT was applied. Therefore, the rotor was not trimmed to measured thrust coefficient.

Figure 9.12 presents exemplary numerical validation for all considered forward flight cases in terms of C_n vs ψ based on integration of pressure distributions at cross-sections of the blade $r/R = 0.75$. The agreement with flight test data is satisfactory for the whole range of forward velocities analyzed. The maximum values of C_n appearing at the retreating side are well predicted by CFD. Some detailed features of the flow presented in flight test data are well reproduced by computations (for example, local maxima of C_n close to $\psi = 90°$ for the low-speed case) (Tejero et al. 2016b).

Figure 9.13 presents the *Cp* distributions for the high-speed marker for different cross-sections and azimuthal positions. The shock wave present at $r/R = 0.86$ and $\psi = 90°$ is well predicted by the numerical simulations. Besides, the two shocks (suction and pressure sides) located at $r/R = 0.99$ and $\psi = 90°$ are also reproduced by the numerical simulation. On the other hand, the Cp distribution at the retreating side of the rotor blade ($r/R = 0.96$ and $\psi = 270°$) is well reproduced by CFD.

Only the high-speed marker simulated showed significant flow separation to be controlled by the proposed passive flow control device. Figure 9.14 presents the skin friction coefficient (C_f) at the suction side of the AH-1G helicopter rotor blade (steps of 30°) in high-speed forward flight conditions. To simplify the figure just three colors are showed: blue color represents the areas where the flow is attached

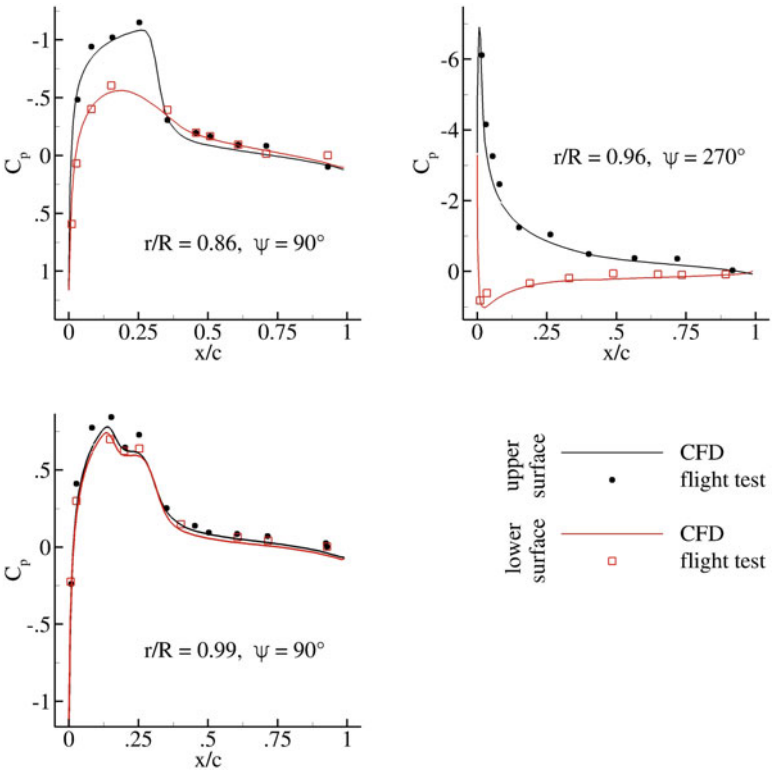

Fig. 9.13 Numerical validation in terms of pressure distribution (Tejero et al. 2016b)

to the rotor blade, the red color presents flow separation (induced by shock waves or dynamic stall), and the green color indicates the areas where the flow is attached to the surface but exerting low shear stress, $Cf < 10-4$ (boundary layer close to separation).

The flow past a helicopter rotor blade in forward flight conditions is highly unsteady and therefore the boundary layer thickness is continuously changing. For this numerical investigation, the RVGs were designed with the flow properties upstream of the shock wave located at $\psi = 45°$ ($\delta = 0.004$c). 18 RVGs were placed on the blade from $r/R = 0.91$ and $r/R = 0.96$ with the following dimensions: $\phi_{\mathrm{RVG}} = \delta/4$, $h = \delta/2$, and $L = 5.0 \times \delta$.

9.4.2.2 Flow Control Case (RVG)

Figure 9.15 presents the disk loads in terms of normal (C_n) and torque (C_q) Mach scaled coefficients. The left side of the figure shows the reference case (no flow control) where it is visible how the normal force is generated by fore and aft parts of

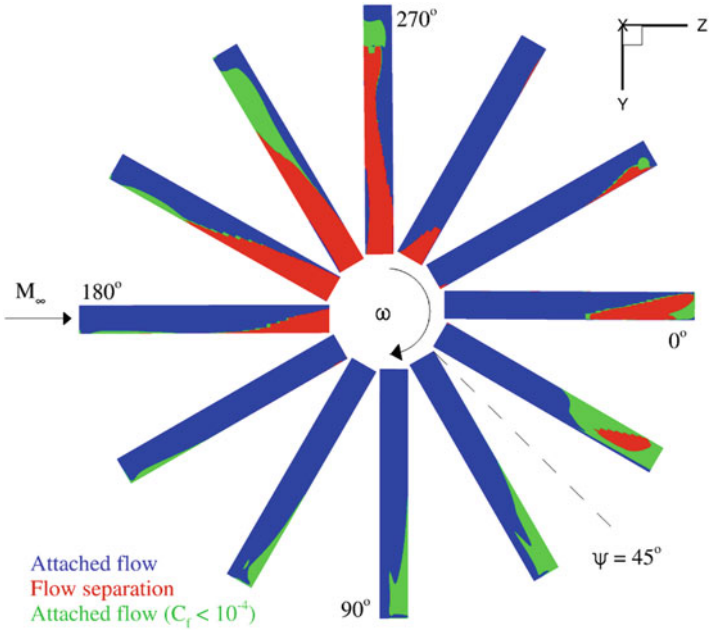

Fig. 9.14 Skin friction coefficient on the suction side of the AH-1G rotor blades in high-speed forward conditions

the rotor disk with negative values at $\psi = 90°$ close to the blade tip due to negative inflow angle and at $\psi = 270°$ close to the blade root caused by the reverse flow area. The torque Mach scaled is mainly generated at the retreating side. The right side of the figure presents the delta of the investigated Mach scaled coefficients (flow control minus reference case). The negative effect of the RVGs (blue) is visible only near $\psi = 0°$, where the flow is massively separated from the leading edge. The rods are most effective between $\psi = 30°$ and $\psi = 60°$, where a strong shock wave induces flow separation. Moreover, an improvement in C_n is also evident for the remaining azimuthal positions. Even in locations not subjected to flow separation, the implementation of RVGs has a beneficial effect on aerodynamic performance, due to an increased value of the skin friction coefficient (improved boundary layer state). More details are described in Tejero et al. (2016a).

The contour map of Mach at the cross-section $r/R = 0.92$ of the azimuthal positions marked in Fig. 9.15 is presented in Fig. 9.16. The first location shows how the massive separation is still present at the retreating side when RVGs are applied. The flow separations start at the leading edge (RVGs are located in a reverse zone area) and the formation of streamwise vortices cannot be expected. On the other hand, the control of the strong shock-wave boundary layer interaction of this flow control system is visible in the second location.

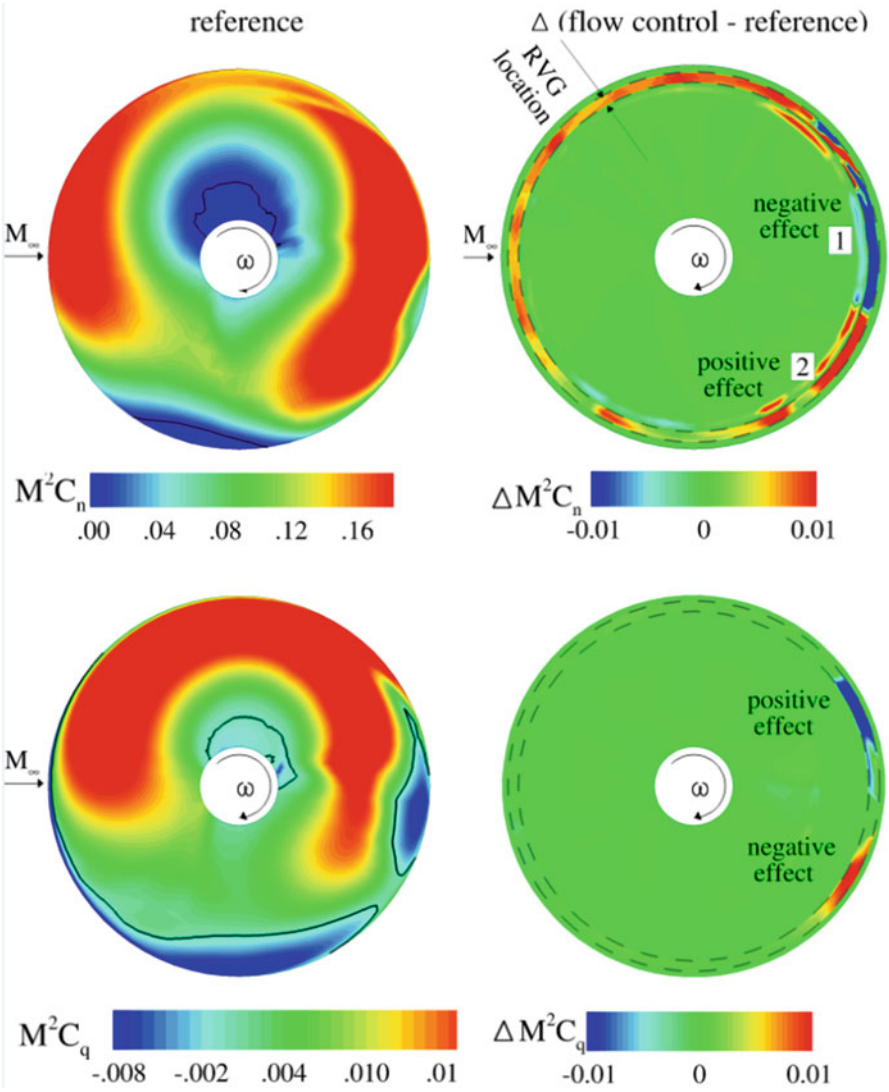

Fig. 9.15 Mach scaled normal force (C_n) and torque (C_q) coefficients for the reference case (*left*) and the influence of RVGs on the rotor disk (*right*) (Tejero et al. 2016a)

The application of RVGs in the AH-1G main helicopter rotor blade leads with an enhancement by 2.6 % in the thrust coefficient with a drag penalty induced by the rods (visible in the increment of power consumption by 1.1 %).

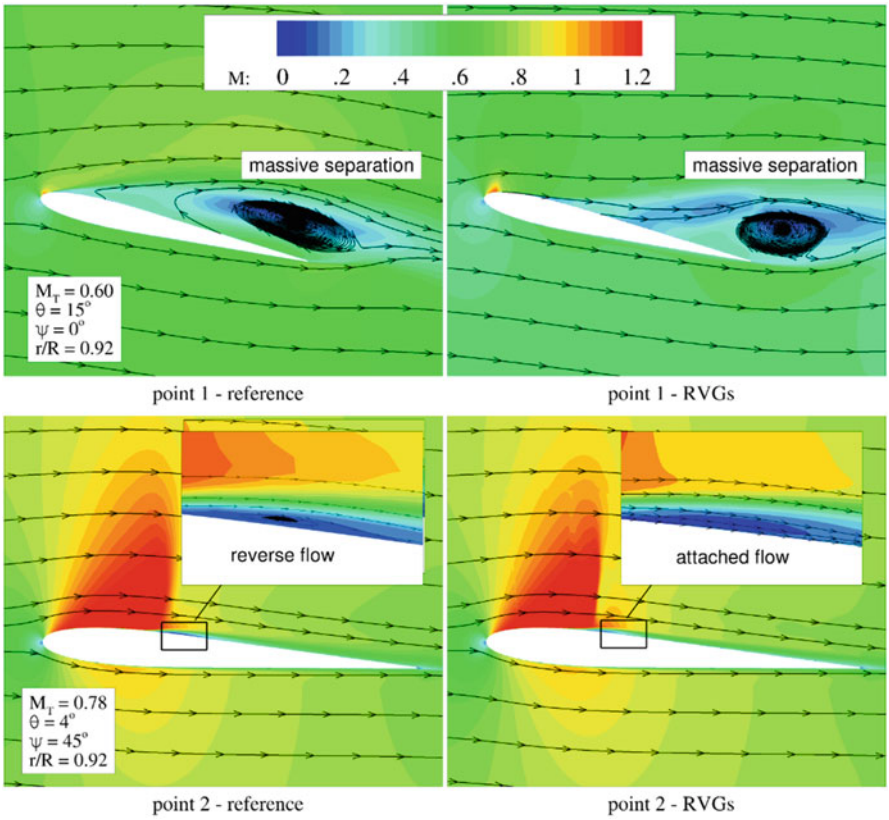

Fig. 9.16 Mach contour map and the influence of RVGs on flow separation on the AH-1G rotor blades in high-speed forward flight conditions (Tejero et al. 2016a)

9.5 Conclusions

The chapter presents the numerical investigation of the possible application of rod vortex generators on helicopter rotor blades. The Caradonna–Tung and AH-1G helicopter rotor blade were investigated in hover and forward flight conditions, respectively. The numerical models were validated with the available experimental data/flight test data. The application of the proposed passive flow control device on the suction side of both rotors leads to a separation control, which enhanced the thrust coefficient. The main drawback of the presented technology is the power consumption penalty associated with its implementation.

References

Ahmad J, Duque EPN (1996) Helicopter rotor blade computation in unsteady flows using moving overset grids. J Aircr 33(1):54–60

Boniface JC (2014) A computational framework for helicopter fuselage drag reduction using vortex generators. In: AHS 70th Annual Forum, Montreal, Canada

Caradonna FX, Tung C (1981) Experimental and analytical studies of a model helicopter rotor in hover. NASA Technical Memorandum 81232

Cross JL, Watts ME (1988) Tip aerodynamics and acoustics test. NASA Reference Publication 1179

Kang HJ, Kwon OJ (2002) Unstructured mesh Navier-Stokes calculations of the flow field of a helicopter rotor in hover. J Am Helicopter Soc 47(2):90–99

Kenning OC, Kaynes IW, Miller JV (2004) The potential application of flow control to helicopter rotor blades. In: 30th European Rotorcraft Forum, Marseilles, France, 14–16

Seddon J, Newman S (2011) Basic helicopter aerodynamics, Aerospace series. Wiley, Hoboken. ISBN 9780470665015

Sheng C (2011) A preconditioned method for rotating flows at arbitrary mach number. Modell Simul Eng 2011:1–17

Tejero F, Doerffer P, Szulc O (2016a) Application of passive flow control device on helicopter rotor blades. J Am Helicopter Soc 61(1):1–13

Tejero F, Doerffer P, Szulc O, Cross JL (2016b) Numerical simulation of the tip aerodynamics and acoustics test. J Therm Sci 25(2):153–160

Yang Z, Sankar LN, Smith M, Bauchau O (2002) Recent improvements to a hybrid method for rotors in forward flight. J Aircr 39(5):804–812